HHS Public Access

Author manuscript

Mol Cell. Author manuscript; available in PMC 2016 January 06.

Published in final edited form as:

Mol Cell. 2015 March 19; 57(6): 1110–1123. doi:10.1016/j.molcel.2015.02.016.

Mn^{2+}-Sensing Mechanisms of *yybP-ykoY* Orphan Riboswitches

Ian R. Price[1], **Ahmed Gaballa**[2], **Fang Ding**[1], **John D. Helmann**[2], and **Ailong Ke**[1,*]

[1]Department of Molecular Biology and Genetics, 253 Biotechnology Building, Ithaca, NY 14853, USA

[2]Department of Microbiology, Wing Hall, Cornell University, Ithaca, NY 14853

Summary

Gene regulation *in cis* by riboswitches is prevalent in bacteria. The *yybP-ykoY* riboswitch family is quite widespread, yet its ligand and function remained unknown. Here we characterize the *Lactococcus lactis yybP-ykoY* riboswitch as a Mn^{2+}-dependent transcription-ON riboswitch, with a ~30–40 μM affinity for Mn^{2+}. We further determined its crystal structure at 2.7 Å to elucidate the metal sensing mechanism. The riboswitch resembles a hairpin, with two coaxially stacked helices tethered by a four-way junction and a tertiary docking interface. The Mn^{2+}-sensing region, strategically located at the highly conserved docking interface, has two metal binding sites. Whereas the one site tolerates binding of both Mg^{2+} and Mn^{2+}, the other site strongly prefers Mn^{2+} due to a direct contact from the N7 of an invariable adenosine. Mutagenesis and a Mn^{2+}-free *E. coli yybP-ykoY* structure further reveal that Mn^{2+} binding is coupled with stabilization of the Mn^{2+}-sensing region and the aptamer domain.

Introduction

Ligand-dependent regulation by riboswitches is an important gene regulatory mechanism, particularly in prokaryotes. These RNAs usually reside in 5′ untranslated regions (5′-UTRs) of mRNAs and regulate expression mainly by premature transcription termination or inhibition of translation initiation (Peselis and Serganov, 2014; Price et al., 2014; Serganov and Nudler, 2013). Other regulatory mechanisms have been demonstrated, including the control of mRNA degradation or alternative splicing (Caron et al., 2012; Li and Breaker, 2013). Over two dozen classes of riboswitches have been experimentally validated (Breaker, 2011). The ligand identities and regulatory functions of many more classes of riboswitches remain obscure, thus they are “orphans” (Barrick, 2004; Weinberg Z, 2010).

The *yybP-ykoY* motif constitutes the fourth most common riboswitch class known, yet it has remained an orphan (Argaman, 2001; Barrick, 2004; Meyer et al., 2011). This is primarily

*Corresponding author: Dr. Ailong Ke, ailong.ke@cornell.edu, 607-255-3945.

Author Contributions

IRP performed IVT, SHAPE, RNA purifications, and X-ray crystallography, FD performed part of RNA purification and crystallization. AG performed all in vivo work, including the LacZ expression assay and YoaB Mn^{2+} rescue experiments. Each author contributed to the manuscript preparation.

Accession Numbers

The coordinates and the structure factors for the *L. lactis* Mn^{2+}-bound, A41U mutant, and the *E. coli* Mn^{2+}-free *yybP-ykoY* riboswitch structures have been deposited in the Protein Data Bank with accession codes 4Y1I, 4Y1J, and 4Y1M, respectively.

because its associated genes have been uncharacterized, including *yybP* and *ykoY*, the two genes in *Bacillus subtilis* after which this riboswitch class was named (Barrick, 2004). Sequence analysis reveals that the putative *yybP-ykoY* aptamer domain is often mutually exclusive with a predicted transcription terminator structure, which suggests that aptamer stabilization will serve to up-regulate gene expression by disrupting the terminator structure (Barrick, 2004). The *yybP-ykoY*-containing RNA SraF, associated with the gene encoding the TerC family member *alx* in *E. coli* (Argaman, 2001), was previously identified as a pH-responsive "riboregulator" (Nechooshtan et al., 2009). However, the pH response required sequences outside the *yybP-ykoY* consensus that are not present in most instances (Nechooshtan et al., 2014; Nechooshtan et al., 2009). Thus, the *yybP-ykoY* motif itself may have a different role.

More recently, one *yybP-ykoY* associated gene product, YebN (also called MntX and MntP), was independently implicated as a Mn^{2+} efflux pump in *Xanthomonas oryzae* (Haller et al., 2011), *E. coli* (Waters, 2011), and *Neisseria meningitidis* (Veyrier, 2011). Furthermore, multiple instances of the *yybP-ykoY* motif are found in regions that also contain predicted binding sites for MntR or Fur family transcription factors, which are involved in Mn^{2+} and other metal homeostasis (Lee and Helmann, 2007; Waters, 2011).

Based on these observations, we hypothesized that *yybP-ykoY* riboswitches may sense elevated levels of Mn^{2+} and in turn up-regulate genes related to Mn^{2+} homeostasis. In this work, we present several lines of evidence suggesting that a *Lactococcus lactis yybP-ykoY* riboswitch, found upstream of the *yoaB* gene, functions as a transcription-ON Mn^{2+}-responsive riboswitch. The riboswitch binds Mn^{2+} with an effective K_d of ~30–40 μM, as monitored by both an *in vitro* transcription (IVT) assays and selective 2′-hydroxyl acylation analyzed by primer extension (SHAPE), and mediates gene induction specifically by elevated Mn^{2+} as monitored in *B. subtilis*. These regulatory effects were not observed for other metals. The crystal structure of the *L. lactis yybP-ykoY* riboswitch aptamer domain bound to Mn^{2+} reveals the Mn^{2+}-binding selectivity mechanism, which is validated by both functional and structural analysis of binding site mutants, and is supported by comparison with the structure of the Mn^{2+}-free *E. coli yybP-ykoY* riboswitch. The identification of *yybP-ykoY* as a Mn^{2+} riboswitch has implications for the functions of its uncharacterized associated genes as well as for metal homeostasis. To this end, we provide physiological evidence to suggest that a previously uncharacterized P-type II ATPase (YoaB) in *L. lactis* functions as a Mn^{2+} exporter.

Results

The *L. lactis yybP-ykoY* riboswitch is Mn^{2+}-responsive both *in vitro* and *in vivo*

Because *yybP-ykoY* riboswitch-associated genes in *X. oryzae*, *E. coli*, and *N. meningitidis* were implicated as Mn^{2+} efflux pumps (Haller et al., 2011; Veyrier, 2011; Waters, 2011), we hypothesized that the function of this orphan riboswitch family could be to specifically bind Mn^{2+} and regulate expression of proteins important for Mn^{2+} homeostasis. An IVT assay was used to test this hypothesis using the putative transcriptional *yybP-ykoY* riboswitch upstream of the *L. lactis yoaB* gene, which encodes a predicted P-type II (calcium-transporting) ATPase (Figure. 1A). The P1.1 helix of this *yybP-ykoy* aptamer is

found mutually exclusive with a predicted intrinsic transcription terminator. This riboswitch was shown to specifically respond to Mn^{2+} concentration in this assay (Figure. 1B). RNA polymerase produced predominantly terminated transcripts in the absence of Mn^{2+}. Addition of 0.5 mM Mn^{2+}, but not other metals tested (Fe^{2+}, Co^{2+}, Ni^{2+}, and Ca^{2+}), led to highly efficient anti-termination, presumably because Mn^{2+}-induced stabilization of the aptamer domain disrupted the terminator structure (Figure 1A). IVT under a range of Mn^{2+} concentrations further revealed a half-maximal response of 40+/−15 μM(Figure 1C). This value is possibly influenced by both thermodynamic parameters (e.g. effective K_d) and kinetic factors (e.g. RNA folding and RNA polymerase rate) within its folding window (Quarta et al., 2012). High concentrations (10 mM) of Mg^{2+} could also induce transcription read-through (data not shown), presumably by favoring the bound-like aptamer structure, a typical observation in diverse riboswitch families (Hennelly et al., 2013; Holmstrom et al., 2014; Santner et al., 2012). The metal ion selectivity for Mn^{2+} over Mg^{2+} is at least 200-fold based on apparent binding constants as judged by this assay.

Next, we used SHAPE chemical probing to determine if the observed anti-termination activity was correlated with any Mn^{2+}-induced conformational changes in the aptamer domain, as opposed to acting through RNA polymerase (Figure 1D). The observed reactivity pattern confirmed the bioinformatically predicted secondary structure (Barrick, 2004) (Figure 1A) in solution. Notably, the U87-A88 (4-way junction) region displayed prominent Mn^{2+}-dependent protection, with more modest changes across L1 (bases 7–12, 91–94), L3 (39–45), and the base of P1 (1–6, 100). Based on the SHAPE reactivity change at the U87-A88 residues, the Mn^{2+} binding K_d was estimated to be ~27+/−6 μM (Figure 1E). This parameter, obtained independent of the kinetic factors present during transcription, is roughly comparable to the value derived from the transcription assay.

To determine if this riboswitch can also mediate Mn^{2+}-dependent regulation *in vivo*, we fused the *L. lactis yoaB* leader region (containing the *yybP-ykoY* riboswitch) to the *lacZ* gene and monitored metal activation of gene expression in *B. subtilis*. Since Mn^{2+} import is tightly regulated in wild-type *B. subtilis* by the MntR repressor, we used an *mntR* mutant strain that constitutively expresses Mn^{2+} uptake transporters to measure the cellular response to Mn^{2+} excess (Que and Helmann, 2000). In this genetic background, addition of 1 to 10 μM Mn^{2+} to the LB growth medium activated expression of *β*-galactosidase several-fold (Figure 1F). These levels of Mn^{2+} are sufficient to inhibit growth (Que and Helmann, 2000) and elicit Mn^{2+}-stress as visualized at the level of the transcriptome (Guedon et al., 2003). In contrast, addition to the medium of other metals (400 μM Cu^{2+}, Ni^{2+}, Co^{2+}, Mg^{2+} or Fe^{2+}) had little if any effect on expression (Figure 1F, Figure S7). Together, these results demonstrate that this riboswitch can function as a Mn^{2+}-specific genetic ON-switch both *in vitro* and *in vivo*.

Crystal structure of the Mn^{2+}-bound *L. lactis yybP-ykoY* family riboswitch

Mn^{2+} and Mg^{2+} have similar ionic radii, metal coordination schemes, and charges. Whereas Mg^{2+} is present at low mM concentration inside cells (Grubbs, 2002), Mn^{2+} is typically maintained at levels 10- to 100-fold lower (Helmann, 2014). Therefore it is a particularly challenging task for RNA to selectively sense Mn^{2+}. Other transition metals inside the cell

further complicate the situation. To fully understand the mechanism of selective Mn^{2+} sensing, we determined the crystal structure of the Mn^{2+}-bound *L. lactis yybP-ykoY* riboswitch at 2.85 Å resolution (Figures 2A, 2B, S1A; Table 1). The base pairing observed nicely matches that predicted by comparative genomic studies (Barrick, 2004) and SHAPE, with all elements present. The two molecules in the crystal asymmetric unit exhibit almost identical conformations (total RMS = 0.58 Å). The four helices organize into two coaxially stacked superhelices (P1–P2 and P3–P4) tethered by a four-way-junction (4WJ), resembling an overall hairpin shape. The two "legs" of the hairpin dock together at the highly-conserved L1 and L3 loops (Figure 2C, D). The centrality of these conserved sequences in the overall structure is demonstrated in Figure S1B. This interface is stabilized primarily by two highly coordinated metal ions, which bind at an intricately arranged pocket. Specifically, the L1 loop contains four layers of non-Watson-Crick (WC) interactions: a sheared G7•A94 pair [sugar (S)-Hoogsteen (H)], a G8•G93 pair (WC-H), a G19•U11•A92 base triple, and a weak A12•A91 (WC-S) pair (Figure 2C). These interactions fulfill two functions: 1) to flip out the absolutely conserved A9 residue, which undergoes a cross-helix Type I A-minor interaction with the conserved C37-G60 pair in P3.1 and also base stacks with the top of L3 (Figures S1E, 2C); and 2) to twist the backbone of G7-A9 to orient the three phosphates towards each other, creating a metal ion binding hotspot (Figure 2C). On the opposite side of the binding interface, L3 (U39-C45) is extruded from the stacking lattice between P3.1 and P3.2. The L3 backbone twists, pointing the phosphates of U39-C40 and U44-C45 inward to accommodate the metal ions at the L1-L3 interface (Figure 2D). The L3 conformation is stabilized in part by base stacking, which nucleates at A9 in L1 and propagates to U39, C40, A41, C45, U44, and A42 (Figure 2D); stacking between C40 and A41 is in a tilted fashion. N4 of the highly conserved C40 appears to make a hydrogen bond to the 2′-OH of G46 in P3.2. U43 is flipped out and mediates a sharp U-turn (Figure 2D). Overall, the crystal structure nicely explains the observed sequence conservation and the SHAPE Mn^{2+}-dependent reactivity profile.

The molecular basis of Mn^{2+}-sensing

Besides the A-minor motif interaction, L1 and L3 lack residue-specific inter-loop interactions. Most of the docking affinity appears to originate from the inner-sphere coordination of two metal ions (M_A and M_B) at the interface. M_A is coordinated in an octahedral fashion by five inner-sphere phosphoryl oxygen atoms from residues in L1 (G7, G8, and A9) and L3 (U39 and C45) (Figures 2E, S1C-D), and by a water molecule hydrogen bonded to the phosphate of G38. In contrast, while M_B is also coordinated octahedrally, one of its six ligands is N7 of the invariable A41 in L3, with the rest of its ligands being phosphoryl oxygen atoms of G8, U39, C40, U44, and C45. In addition to the N7-Mn^{2+} contact, A41 further positions itself by donating a hydrogen bond from its N6 primary amine to the phosphoryl oxygen of U39.

It is well-established that both Mg^{2+} and Mn^{2+} prefer octahedral coordination with similar metal-ligand distances (2.08 versus 2.19 Å, respectively) (Harding and Hsin, 2014). However, Mg^{2+} strongly prefers coordination by hard ligands (i.e. oxygen) whereas Mn^{2+} tolerates softer ligands such as nitrogen and sulfur (Chen et al., 1997; Harding and Hsin, 2014). Therefore, we hypothesized that under physiological conditions (mM Mg^{2+} versus

μM Mn^{2+}), M_A is predominantly occupied by Mg^{2+} due to its abundance, whereas the M_B site will display strong selectivity for Mn^{2+}. The selective binding of Mn^{2+} at the strategic location of the riboswitch docking interface in turn rationalizes the Mn^{2+}-dependent folding behavior of the *yybP-ykoY* riboswitch aptamer domain.

To test this hypothesis, we turned to the anomalous scattering property of Mn to unambiguously assign the identity of these two metal ions. Because Ba^{2+} was indispensable for crystallization and strongly contributes to anomalous scattering at and below the Mn K absorption edge energy, we compared the anomalous differences in datasets collected at and far below this Mn absorption edge (Table 1). Mn anomalous difference peaks are expected to be strong in the Mn-edge map, but very weak in the lower energy map, whereas Ba anomalous peaks are expected to be more consistent between these two maps. Mg^{2+} has no observable anomalous diffraction at these energies. With artificially high (2.5 mM) Mn^{2+} present in the crystallization buffer, the anomalous difference map at the Mn edge revealed high occupancy for both the M_A and M_B sites (Figure S2A, B). However, below the Mn edge, there is no anomalous difference at either site (Figure S2A), suggesting that Ba^{2+} does not bind there. Peaks in more open positions outside the L1-L3 region (presumably due to Ba^{2+}) appear in both maps. These results are consistent with Mn^{2+} occupying both the M_A and M_B sites at mM concentration. The exclusion of large Ba^{2+} ions from M_A and M_B suggests that the metal sensor region may also be sensitive to the ionic radii (or preferred geometry) of ions as an additional discrimination mechanism. Significantly, at lower (100 μM) Mn^{2+}, the anomalous difference map at the Mn-edge contained a strong peak at M_B, but dramatically reduced occupancy at M_A (Figure 2E), suggesting that, at the physiological concentration ranges, Mn^{2+} selectively occupies M_B site. This supports the hypothesis that the M_B site is the main factor in determining Mn^{2+} selectivity over Mg^{2+}.

Structure-guided mutagenesis of the *L. lactis yybP-ykoY* riboswitch confirms functional elements

Next, mutations followed by SHAPE and IVT assays were used to test the roles of specific structural features. Several base-substitutions targeted the L1 loop, the most conserved region in the *yybP-ykoY* riboswitch. The A9C and U11A substitutions target the cross-helix A-minor contact and a nearby conserved G11•U12•A93 base triple, respectively. Both substitutions resulted in a catastrophic unfolding of the riboswitch, with increased SHAPE reactivities at L1, L3, and the four-way junction (4WJ), with concomitant loss of the Mn^{2+} response (Figure 3A). An A12U substitution converts the sheared A12•A91 pair in L1 to a U-A pair. This substitution has surprisingly little effect on structural integrity; whether this base pair is involved in fine-tuning the switching behavior of the riboswitch awaits further investigation. C40 and A41 are the two most conserved residues in L3. The C40U substitution lost the Mn^{2+}-dependent response, displayed moderately increased flexibility in L3 (consistent with the importance of its H-bond to the 2′-OH of G46), and had higher reactivity near the 4WJ as a secondary effect (Figure 3A). The invariant A41 is responsible for the selective binding of Mn^{2+} to the M_B site through an N7-Mn^{2+} contact. We predict that this contact is likely replaced by a coordination to M^{2+} by O4 group of U41, resulting in a loss-of-selectivity phenotype. The A41U RNA still displayed Mn^{2+}-induced response at the 4WJ region. However, the Mn^{2+}-dependent protections at L1 and L3 were less

prominent, and an extra hyper-reactive band appeared at U43 in L3, suggesting that this loop adopts a significantly different conformation (Figure 3A). The increased reactivity in the L3 and 4WJ of the A41U mutant may also be due to the loss of stabilization by the H-bond between the A41 exocyclic amine and the non-bridging phosphoryl oxygen from G46, or because of decreased base stacking stability by A41U substitution. While the A41G mutant maintains N7, substitution of the N6 primary amine in adenosine with the O6 carbonyl of a guanosine at position 41 would disrupt the H-bond to the backbone of G46. Indeed, the L3 loop in the A41G mutant RNA is significantly more flexible, and the Mn^{2+}-dependent changes are lessened.

Full-length riboswitch with A41G or A41U mutations were also tested by IVT. Each required ~3-fold higher [Mn^{2+}] to drive the same level of read-through transcription as the wild-type, suggesting that their metal sensitivity is impaired (Figure 3B). Overall, these mutational studies validate the conclusions from the structural analysis.

The structure of the A41U mutant riboswitch reveals an altered metal coordination scheme

To further investigate the effect of the A41U substitution on the metal sensitivity of the riboswitch, we determined its crystal structure at 2.2 Å resolution in the presence of 2.5 mM Mn^{2+}, 10 mM Mg^{2+}, and 80 mM Sr^{2+} (Figure 3C; Table 1). The overall structure of this mutant aligns well with the wild-type, with an r.m.s.d of 1.7 Å for all phosphorus atoms. However, the L3 loop in the metal sensing region displays significant local differences (Figure 3D) and as a result, loses selective recognition of Mn^{2+} at the M_B site. Specifically, the backbone of U41-U44 is shifted, disrupting the extensive base stacking observed in the wild-type structure (Figure 3D, gray). A42 and U43 were also more flexible, as evidenced by their weaker electron densities. Furthermore, the two molecules in the asymmetric unit of the mutant crystal vary in this region, particularly at residue A42 (Figure S3A). These observations echo the increased flexibility deduced by SHAPE at bases 42–45 in the mutant. Whereas M_A coordination remains the same as in the wild-type, the A41U mutation and the subsequent changes in L3 conformation altered the metal coordination scheme at the M_B site. It shares four of the phosphoryl oxygen contacts observed in the wild-type M_B (G9, U39, C40, and C45). However, the backbone phosphate at U44 is shifted away and replaced by a water, which is clearly resolved in the 2.2 Å electron density (Figure 3D). The A41U substitution replaces the adenine N7-metal contact with a uracil O4-metal interaction, which approaches from a slightly different direction. Judging by the increased metal-ligand distance (mostly 2.0–2.2 Å in the wild-type but ~2.4 Å in the mutant), and the coincidence of two Sr anomalous difference peaks at both sites (Figure S3B), we interpret that both M_A and M_B are mostly occupied by Sr^{2+} due to its significant presence in the mutant riboswitch crystal, even though 2.5 mM Mn^{2+} was also present. These findings support the conclusion that the A41U RNA has reduced specificity for Mn^{2+}.

The L3 loop sensor region melts in the Mn^{2+}-free crystal structure

Having observed one Mn^{2+} and one primarily Mg^{2+} ion in the metal sensor region, we wished to determine if these two metal ions bind independently or cooperatively of one another. One way to address this is to compare the Mn^{2+}-bound structure with the Mn^{2+}-free counterpart. Efforts to capture a Mn^{2+}-free structure were unsuccessful for the *L. lactis*

yybP-ykoY riboswitch. Therefore, we expanded our efforts to homologs and successfully determined a 3.0 Å structure of the *E. coli yybP-ykoY* riboswitch in the Mn^{2+}-free state. The overall architecture of these two riboswitches is similar (Figure 4A, Figure S4, Table 1). In both structures, a metal ion is coordinated by the equivalent phosphoryl oxygens at the M_A site, consistent with the proposal that this site is occupied by Mg^{2+} at physiological conditions. However, the M_B site is largely collapsed in both monomers in the Mn^{2+}-free *E. coli* structure, lacking metal occupancy (Figures 4C, S4). This confirms the assignment of M_B as the Mn^{2+} specific sensing site, and suggests that folding around the Mn^{2+} binding site is dynamic and Mn^{2+}-dependent. In fact, residues A47-U51 in the *E. coli* L3 loops are in completely different conformations than their equivalent residues (A41-U45) in the *L. lactis* structure (Figure 4C). Additionally, this region is partially stabilized by a crystal contact in one monomer in the asymmetric unit of the crystal (molecule B), but is mostly disordered in the other monomer (molecule A) lacking such a crystal contact (Figure S4). Overall, this structural comparison suggests that the M_A site may be occupied even in the absence of Mn^{2+} (presumably by Mg^{2+}). However, as suggested by the SHAPE analysis, Mg^{2+} binding alone is not sufficient to stabilize the inter-domain binding interface, and further binding of Mn^{2+} to M_B is required. Without it, L3 becomes largely unstructured and L1 and P1.1 may be more prone to unfolding. The series of local conformational changes may propagates to trigger the formation of the alternative (termination) structure. A more careful conformational dynamics study is required to fully define these equilibria and any role of RNA folding kinetics in the decision making process of this riboswitch.

The *L. lactis yybP-ykoY* riboswitch regulates a P-type ATPase that protects cells against Mn^{2+} toxicity

The *yybP-ykoY* motif is associated with a number of genes (Meyer et al., 2011), most of which are heretofore uncharacterized (Figure S5). The finding that the *yybP-ykoY* element functions as a Mn^{2+}-sensing riboswitch provides hints for future functional characterization of these genes. Since the *L. lactis yybP-ykoY* riboswitch regulates a predicted P-type ATPase (YoaB), we predicted that it would function as a Mn^{2+} efflux pump like YebN (Haller et al., 2011). To test this hypothesis, we tested the ability of YoaB to rescue Mn^{2+} sensitivity in *B. subtilis* using a zone-of-inhibition assay (Figure 5).

The *yoaB* gene was amplified from *L. lactis* and integrated into the *B. subtilis* genome under the control of an inducible promoter. Induction of YoaB synthesis in wild-type cells led to only a modest increase in resistance to Mn^{2+}. However, wild-type *B. subtilis* is highly resistant to Mn^{2+} (at least 1 mM is required to inhibit growth) due to the tight repression of the two main Mn^{2+} uptake systems (MntH and MntABC) by the MntR repressor (Helmann, 2014). An *mntR* mutant strain constitutively expresses Mn^{2+} uptake transporters and therefore provides a suitable background for monitoring the ability of the putative YoaB efflux pump to confer Mn^{2+} resistance. As expected, the *mntR* mutant displayed a greatly increased zone of growth inhibition compared to wild-type. Significantly, this Mn^{2+} sensitivity could be largely rescued by induction of YoaB (Figure 5). This is consistent with the expectation that the P-type ATPase, which is specifically induced by Mn^{2+}, serves to export Mn^{2+} from cells, although future biochemical experiments will be required to test this hypothesis.

Discussion

The lack of identification of the physiologically relevant regulatory ligands for orphan riboswitches presents a major barrier to understanding the roles of these RNA elements and, by extension, the many proteins under their control. Here, we demonstrate that the *yybP-ykoY* RNA motif is a Mn^{2+} riboswitch as monitored both *in vitro* and *in vivo*. Structural analyses, especially the comparison of the Mn^{2+} bound and free structures, provide insights into the series of molecular events leading to the Mn^{2+}-dependent switching behavior. The ability of RNA to selectively discriminate and respond to Mn^{2+} in the cellular environment is remarkable in light of the fact that the chemically similar Mg^{2+} ion is present at millimolar levels in cells (Grubbs, 2002) (10- to 100-fold higher than Mn^{2+}), and Mg^{2+} is widely appreciated for its ability to bind RNAs both as a general counterion and in specific binding pockets. Our structural studies reveal that Mn^{2+} sensing in *yybP-ykoY* is ultimately decided by the binding of a single Mn^{2+} ion at a strategic location of the riboswitch. In order to distinguish Mn^{2+} from a sea of Mg^{2+} and transition state metal ions, the *yybP-ykoY* riboswitch first creates two phosphate-rich pockets that attract metal ions. The metal binding process is apparently ion-radius sensitive (rejection of the large Ba^{2+}), and is coupled with a complete dehydration process. Complete metal ion dehydration is rarely observed in RNA structures. It usually only occurs in the ‘business center’ of a structured RNA, such as in the active sites of the self-cleaving group I and II introns (Stahley and Strobel, 2005; Toor et al., 2008). The side-by-side, yet highly selective binding of a Mn^{2+} and a Mg^{2+} in *yybP-ykoY* is unprecedented and showcases the ability of RNA to discriminates Mn^{2+} from Mg^{2+}. After dehydration, the *yybP-ykoY* riboswitch exploits the ability of Mn^{2+} to tolerate a softer ligand, the N7 of an absolutely conserved adenosine, among hard oxygen ligands in its octahedral coordination sphere, to sense the relative ‘hardness’ of the metal ions. The conformation dynamics of the riboswitch are fine-tuned, such that the conformation of the residues surrounding the Mn^{2+} binding site, and the stability of the docking interface, are critically dependent on Mn^{2+} binding. It is not a coincidence that the alternative structure formation nucleates from the melting of the P1.1 helix (Figure 1A), as this region appears to be the most dynamic structure element in the *yybP-ykoY* riboswitch, bearing weakened electron density in the Mn^{2+}-bound structure (Figure S1A), and adopting multiple conformations in the Mn^{2+}-free structure (Figure S4). Discrimination from other metal ions is likely based collectively on their charge, intracellular free concentration, preferred coordination geometry and ligand hardness, and possibly ionic radius (in the case of Ba^{2+} rejection by *L. lactis*). Riboswitches responding to other transition state metal ions may exist, and function along the same principle, by dehydrating the metal ion first and chelating it with functional groups to satisfy the preferred coordination geometry and ligand hardness. Overall, the Mn^{2+} sensing mechanism in the *yybP-ykoY* riboswitch is conceptually similar to that of the fluoride riboswitch (Ren et al., 2012), where a single ion influences the stability of the riboswitch, but distinct from that of the M-box Mg^{2+} riboswitch, where multiple ions collectively influence the stability of the riboswitch structure (Dann et al., 2007).

Interestingly, the overall architecture of this riboswitch broadly resembles that of the hairpin ribozyme at two levels (Fedor, 2000) (Figure S6). This starts at the overall shape of the RNA, with two helical stacks connected at a four-way junction, except that the two helical

stacks are more parallel and further apart in the Mn^{2+} riboswitch. Secondly, a cross-helix tertiary contact distal to the 4WJ further rigidifies the hairpin conformation. It is a guanosine flip-out in the hairpin ribozyme that mediates cross-helix interactions to bring reactants into their correct orientation and distance for the self-cleavage reaction. The same base flip-out mechanism is present in the Mn^{2+} riboswitch (Figure S6), however, the cross-helix contact is significantly more extensive. The Mn^{2+}-dependent stability of this docking interaction between L1 and L3 in *yybP-ykoY* critically influences the functional decision of the riboswitch, by preventing unfolding of P1.1 to allow terminator formation. We hypothesize that, similar to the scenario in the hairpin ribozyme system (Zhuang et al., 2002), multiple conformational intermediates are involved in switching on the *yybP-ykoY* riboswitch, this is likely initiated by the cross-helix A-minor docking, and then strengthened by sequential binding of the two metal ions M_A and M_B (comparing Mn^{2+}-free versus -bound structures; Figure 4A). While M_A is unselective and thus is most likely Mg^{2+} *in vivo*, M_B is highly selective for Mn^{2+}. This overall model is depicted in Figure 6. Further study of the conformational dynamics of this riboswitch is necessary to establish the thermodynamic and kinetic framework for this riboswitch.

Our results may be reconciled with the previous characterization of the SraF/Alx leader as pH-responsive riboregulator in several ways (Argaman, 2001; Nechooshtan et al., 2014; Nechooshtan et al., 2009). As mentioned, the pH response required additional sequence that does not appear with most instances of the *yybP-ykoY* motif. Additionally, these studies actually found that Mn^{2+} elicited a transcriptional response, though it was interpreted as due to effects of Mn^{2+} on the pausing dynamics of RNA polymerase (Nechooshtan et al., 2009). In light of the specific recognition of Mn^{2+} by the *yybP-ykoY* riboswitch shown in our work, this may be re-interpreted as Mn^{2+} acting directly through binding to the RNA. Interestingly, the original *in vivo* detection of the SraF (*Alx*-associated) RNA in *E. coli* was found at what we now expect to be the terminated size (Argaman, 2001).

The definition of the *yybP-ykoY* riboswitch as a Mn^{2+} responsive element enables improved functional predictions for the many genes regulated by this element. As a start, we demonstrate that the *L. lactis* YoaB protein, which our IVT and *in vivo* experiments predicted to be induced by Mn^{2+}, confers resistance to elevated levels of Mn^{2+} when expressed in a Mn^{2+}-sensitive *B. subtilis* strain. Since YoaB is bioinformatically predicted to be a P-type II ATPase, our results are consistent with it functioning as an ATP-driven Mn^{2+} efflux pump. Other examples of this riboswitch family are also associated with genes encoding candidate metal pumps or other proteins with probable functions in metal ion homeostasis. In general, bacteria differ tremendously in their preference for Mn^{2+}. Some bacteria, such as *E. coli*, seem to import relatively little Mn^{2+}, although uptake may be induced by oxidative stress (Imlay, 2014) or during host iron limitation (Skaar, 2010). *B. subtilis*, on the other hand, requires Mn^{2+} for growth and maintains cytosolic levels estimated to be in the range of ~10 μM (Ma et al., 2012). *L. lactis* is representative of a small subset of bacteria (the lactic acid bacteria) that have largely dispensed with iron-dependent functions and have a very high cellular demand for Mn^{2+} (Archibald and Duong, 1984). It therefore seems likely that an efflux pump that protects *L. lactis* against Mn^{2+} toxicity may have a lower affinity for Mn^{2+} than the functionally equivalent proteins from organisms that

maintain lower cytosolic Mn^{2+} levels. We speculate that this may be one reason why YoaB does not fully protect *B. subtilis* against Mn^{2+} toxicity. It will also be interesting to explore the natural variation of *yybP-ykoY* riboswitches in terms of their metal sensitivity, which likely correlates with the extent to which various bacteria prefer Mn^{2+} or with different thresholds of expression for the associated proteins. Additionally, the characterization of the *yybP-ykoY* aptamer as a Mn^{2+}-sensitive folding RNA may allow the development of RNA-based Mn^{2+} sensors (Filonov et al., 2014). This will provide a tool for monitoring the real-time fluctuations in free Mn^{2+} levels associated with changes in expression of uptake and efflux pumps and other homeostasis mechanisms.

Materials and Methods

Constructs and Plasmids

The sequences of the constructs used in the biochemical and crystallization experiments, as well as those of the DNA oligos used in the *in vivo* function analysis, are documented in Table S1.

Selective 2′-hydroxyl acylation analyzed by primer extension (SHAPE)

SHAPE was performed as previously described using the 1m7 derivatization reagent (Grigg et al., 2013; Mortimer and Weeks, 2007; Wilkinson et al., 2006). RNA constructs to be analyzed consisted of the *L. lactis* wild-type aptamer domain flanked by SHAPE flanking sequences (Table S1) (Wilkinson et al., 2006). RNAs were *in vitro* transcribed from PCR templates and purified in the same manner as the crystal constructs. Purified RNAs were diluted to 300 nM in refold buffer (100 mM HEPES pH 8, 1 mM $MgCl_2$, 100 mM NaCl) before 1M7 derivatization as described (Grigg et al., 2013). Reverse transcription of the derivatized RNA was performed with a 5′ Cy5-labeled reverse primer and products were separated on a on a 14% UreaGel. A ddTTP sequencing ladder (not shown) was run alongside the reverse transcripts to help identify bands. For the K_d calculation, the combined intensities of bands around the 4-way junction (indicated on the gel) were quantified for each Mn^{2+} concentration with ImageJ. The data were fit using the Origin 8 data analysis software to the equation: y = min + (max − min)*x/(k + x), where y is intensity, min and max are the minimal and maximal intensities, x is the Mn^{2+} concentration, and k is the apparent K_d.

In vitro transcription termination assays

IVT termination assays were performed as described previously (Blouin and Lafontaine, 2007) with modifications. Constructs consisted of wild-type sequence from the *L. lactis yoaB* 5′ UTR (containing the *yybP-ykoY* aptamer domain and an intrinsic terminator) preceded by the *Bacillus subtilis glyQS* promoter. RNA constructs were designed to initiate with an ApC dinucleotide, with no cytosines in the next 13 nt of transcript. Templates were produced by PCR and spin column purified. To assemble stalled RNA polymerase complexes, a master mix (20 nM template, 100 μM ApC dinucleotide, 1 mM DTT, 5% glycerol, 1 mM $MgCl_2$, 0.15 μCi/μL α-^{32}P ATP, 20 μM unlabeled ATP, 50 μM GTP, 50 μM UTP, and 0.008 U/μL E. coli RNA polymerase holoenzyme (Epicentre)) was incubated at 37° C for 15 min, then moved to ice. For synchronized transcription at each condition, 10 μL

of stalled polymerase was mixed with 1.5 μL 10X metal solution or water on ice, then 1.5 μL of 10X elongation buffer (4.5 mg/mL heparin to prevent reinitiation, 650 μM each of unlabeled ATP/CTT/GTP/UTP, 100 mM Tris pH 7.5, 2 mM DTT, 10% glycerol, 2 mM $MgCl_2$) was added. Reactions were allowed to elongate for another 15 min at 37° C, then 10 μL RNA loading dye was added (95% formamide, 20 mM EDTA pH 8, supplemented with xylene cyanol and bromophenol blue). 10 μL of transcripts were separated by 8% urea denaturing PAGE and analyzed by Phosphorimager. The sizes of the terminated and full-length products were confirmed by RNA ladder (not shown). Bands were quantified with ImageJ and each reaction was converted to the fraction of the total RNA in each reaction that was read through to full length. Since the concentration of ATP in the elongation step was significantly higher than in the initiation/stalling step, each molecule was assumed to be end-labeled and no correction was made for the mass of the transcripts. The data were fit using the Origin 8 data analysis software to the equation: $y = min + (max - min)*x/(k + x)$, where y is the fraction read through, min and max are the minimum and maximum readthrough fractions, x is the concentration of $MnCl_2$, and k is the concentration at which the change in readthrough is half maximal. Each assay was performed at least twice on separate days with similar results.

RNA crystal construct preparation

RNA constructs were cloned and produced as described previously (Grigg et al., 2013; Ke and Doudna, 2004). Sequences were cloned into the pUC19 plasmid and were preceded by a T7 RNA polymerase promoter and followed by the hepatitis δ virus ribozyme (HDV) to produce homogeneous ends. Guanosine residues were added at the beginning of each to increase expression. Plasmid templates for transcription were prepared with Qiagen MegaPrep kits and linearized by restriction digestion after the HDV sequence. 10 mL i*n vitro* transcription reactions were performed as previously (Ke and Doudna, 2004). RNA was then purified by urea denaturing PAGE. The *yybP-ykoY* bands were eluted into water at 4° C overnight. RNA was buffer-exchanged to water and refolded at 2–5 μM by heating at 65° C for 10 min in 15 mL 10 mM Na cacodylate pH 7, 50 mM NaCl, followed by the addition of 10 mM $MgCl_2$ and (when appropriate) 0.1 or 2.5 mM $MnCl_2$. RNA was left at 65° C for an additional 2 min and then placed on ice. Cooled samples were concentrated to 0.2 mM and then used for crystallization.

Crystallization and Data Collection

RNA constructs were screened for crystallization by hanging drop vapor diffusion at 0.1 and 0.2 mM RNA, at 21° C and 4° C, with 0, 0.1, or 2.5 mM $MnCl_2$. Optimized conditions for the *L. lactis* Mn^{2+}-bound *yybP-ykoY* riboswitch were: 0.18 mM RNA refolded with 2.5 mM $MnCl_2$ present, and a mother liquor of: 14% (+/−)-2-methyl-2,4-pentanediol (MPD), 40 mM Na cacodylate pH 7.0, 80 mM NaCl, 20 mM $BaCl_2$, 12 mM spermine tetra-HCl, at 21° C, with 1:2 RNA: mother liquor drop ratio. For phasing, 20 mM Iridium Hexamine (IrHex) and 20% PEG-400 were added to the crystals for 3 h prior to freezing.

The *L. lactis* A41U mutant was refolded in the same manner as wild-type, with 2.5 mM $MnCl_2$ present. It crystallized at 0.1–0.2 mM RNA in ~2 months with a mother liquor of 40

mM Na cacodylate pH 6, 15% MPD, 80 mM $SrCl_2$, 12 mM spermine tetra-HCl at 21° C. Crystals were cryo-protected by addition of 20% PEG-400 directly before freezing.

The optimal *E. coli* Mn^{2+}-free crystal conditions were 0.2 mM RNA solution with a mother liquor of 10% MPD, 40 mM Na cacodylate pH 7, 80 mM $SrCl_2$, 20 mM $MgCl_2$, 12 mM spermine tetra-HCl at 21° C. Native crystals were quickly cryo-protected in mother liquor plus 20% ethylene glycol prior to flash freezing in liquid N_2.

Data were collected at either Cornell High Energy Synchrotron Source (CHESS) or the Advanced Photon Source (APS) 24 ID-C Northeastern Collaborative Access Team (NE-CAT), as indicated in Table 1. Datasets were processed using HKL-2000 (Otwinowski and Minor, 1997) or by XDS (Kabsch, 2010) as part of NE-CAT's RAPD pipeline. The *L. lactis* structure was phased by the single-wavelength anomalous dispersion (SAD) method from iridium using PHENIX AutoSol (Adams et al., 2010). Since Sr^{2+} was in its crystal condition, the *E. coli* apo structure was phased by three wavelength multi-wavelength anomalous dispersion (3W-MAD) using Sr. The hkl2map interface for the SHELX suite was used (Pape and Schneider, 2004; Sheldrick, 2010). Final models were built by alternating rounds of manual building in COOT (Emsley et al., 2010) followed by refinement in phenix.refine. RCrane was also used for some model building (Keating and Pyle, 2012).

Strains construction

Two *L. lactis* strains F01 AS 0043 and FSL W6 0449 were obtained from the Wiedmann lab (Food Science Department, Cornell University). *yoaB* ORF with its 5′-UTR region was amplified from *L. lactis* chromosomal DNA using primers Lactis yoaB-F/R, digested with endonucleases, and cloned into pPL82 under the $P_{spac(hy)}$ promoter (Quisel et al., 2001). Plasmids were linearized by *ScaI* and used to transform *B. subtilis*, where they integrated into the *amyE* locus. To generate promoter *lacZ* fusion, primers Lactis Mn ribo-lacZ-F/R were used to amplify the *yoaB* promoter region including the riboswitch and the coding region of the first 12 aa and cloned in pDG1663 vector (Guerout-Fleury et al., 1996). Plasmid was linearized and integrated into *B. subtilis* at the *thrC* locus.

β-galactosidase activity measurements

For β-galactosidase measurement, two separate colonies were used to inoculate LB media and grown to OD_{600} of 0.3. Cells were treated with different metals and further incubated for 1 hour. Cells were collected and β-galactosidase activity was measured according to Miller (1972) (Miller, 1972).

Disc diffusion assays

Susceptibility to different metals was tested using a disc diffusion assay as described previously (Gaballa et al., 2010). Briefly, 100 µl of mid-exponential phase LB cultures were mixed with 4 ml of soft LB and poured onto solidified 15 ml LB plates. Different volumes (3, 5 and 10 µl) of 0.2M $MnCl_2$ (99.99% pure) were added to a paper filler disc and placed on top of the agar plate. The plates were incubated at 37 °C overnight, and the zone of inhibition was measured. Data are the mean of three independent biological replicates (each tested with at least three concentrations of metals).

Supplementary Material

Refer to Web version on PubMed Central for supplementary material.

Acknowledgments

This work was supported by NIH grants GM086766 and GM 102543 to AK and GM059323 to JDH. This work is based upon research conducted at the NE-CAT beam lines of the APS and supported by an award (RR15301) from the National Center for Research Resources at the NIH. Use of the APS is supported by the U.S. Department of Energy, Of ce of Basic Energy Sciences, under contract no. W31-109-ENG-38. This work is also based on research that was also performed at CHESS; funding by the National Science Foundation [DMR-0936384], using the Macromolecular Diffraction at the CHESS facility (MACCHESS; funded by NIGMS [GM103485]).

References

Adams PD, Afonine PV, Bunkoczi G, Chen VB, Davis IW, Echols N, Headd JJ, Hung LW, Kapral GJ, Grosse-Kunstleve RW, et al. PHENIX: a comprehensive Python-based system for macromolecular structure solution. Acta crystallographica Section D, Biological crystallography. 2010; 66:213–221.

Archibald FS, Duong MN. Manganese acquisition by Lactobacillus plantarum. J Bacteriol. 1984; 158:1–8. [PubMed: 6715278]

Argaman LHR, Vogel J, Bejerano G, Wagner EG, Margalit H, Altuvia S. Novel small RNA-encoding genes in the intergenic regions of Escherichia coli. Curr Biol. 2001; 11:941–950. [PubMed: 11448770]

Barrick JCK, Winkler WC, Nahvi A, Mandal M, Collins J, Lee M, Roth A, Sudarsan N, Jona I, Wickiser JK, Breaker RR. New RNA motifs suggest an expanded scope for riboswitches in bacterial genetic control. Proc Natl Acad Sci USA. 2004; 101:6421–6426. [PubMed: 15096624]

Blouin S, Lafontaine DA. A loop loop interaction and a K-turn motif located in the lysine aptamer domain are important for the riboswitch gene regulation control. RNA. 2007; 13:1256–1267. [PubMed: 17585050]

Breaker RR. Prospects for riboswitch discovery and analysis. Molecular cell. 2011; 43:867–879. [PubMed: 21925376]

Caron MP, Bastet L, Lussier A, Simoneau-Roy M, Masse E, Lafontaine DA. Dual-acting riboswitch control of translation initiation and mRNA decay. Proceedings of the National Academy of Sciences of the United States of America. 2012; 109:E3444–3453. [PubMed: 23169642]

Chen Y, Li X, Gegenheimer P. Ribonuclease P catalysis requires Mg2+ coordinated to the pro-RP oxygen of the scissile bond. Biochemistry. 1997; 36:2425–2438. [PubMed: 9054547]

Dann CE 3rd, Wakeman CA, Sieling CL, Baker SC, Irnov I, Winkler WC. Structure and mechanism of a metal-sensing regulatory RNA. Cell. 2007; 130:878–892. [PubMed: 17803910]

Emsley P, Lohkamp B, Scott WG, Cowtan K. Features and development of Coot. Acta crystallographica Section D, Biological crystallography. 2010; 66:486–501.

Fedor MJ. Structure and function of the hairpin ribozyme. Journal of molecular biology. 2000; 297:269–291. [PubMed: 10715200]

Filonov GS, Moon JD, Svensen N, Jaffrey SR. Broccoli: Rapid selection of an RNA mimic of green fluorescent protein by fluorescence-based selection and directed evolution. J Am Chem Soc. 2014

Gaballa A, Newton GL, Antelmann H, Parsonage D, Upton H, Rawat M, Claiborne A, Fahey RC, Helmann JD. Biosynthesis and functions of bacillithiol, a major low-molecular-weight thiol in Bacilli. Proceedings of the National Academy of Sciences of the United States of America. 2010; 107:6482–6486. [PubMed: 20308541]

Grigg JC, Chen Y, Grundy FJ, Henkin TM, Pollack L, Ke A. T box RNA decodes both the information content and geometry of tRNA to affect gene expression. Proceedings of the National Academy of Sciences of the United States of America. 2013; 110:7240–7245. [PubMed: 23589841]

Grubbs RD. Intracellular magnesium and magnesium buffering. Biometals : an international journal on the role of metal ions in biology, biochemistry, and medicine. 2002; 15:251–259.

Guedon E, Moore CM, Que Q, Wang T, Ye RW, Helmann JD. The global transcriptional response of Bacillus subtilis to manganese involves the MntR, Fur, TnrA and sigmaB regulons. Mol Microbiol. 2003; 49:1477–1491. [PubMed: 12950915]

Guerout-Fleury AM, Frandsen N, Stragier P. Plasmids for ectopic integration in Bacillus subtilis. Gene. 1996; 180:57–61. [PubMed: 8973347]

Haller A, Souliere MF, Micura R. The dynamic nature of RNA as key to understanding riboswitch mechanisms. Acc Chem Res. 2011; 44:1339–1348. [PubMed: 21678902]

Harding MM, Hsin KY. Mespeus--a database of metal interactions with proteins. Methods in molecular biology. 2014; 1091:333–342. [PubMed: 24203343]

Helmann JD. Specificity of Metal Sensing: Iron and Manganese Homeostasis in Bacillus subtilis. The Journal of biological chemistry. 2014; 289:28112–28120. [PubMed: 25160631]

Hennelly SP, Novikova IV, Sanbonmatsu KY. The expression platform and the aptamer: cooperativity between Mg2+ and ligand in the SAM-I riboswitch. Nucleic Acids Res. 2013; 41:1922–1935. [PubMed: 23258703]

Holmstrom ED, Polaski JT, Batey RT, Nesbitt DJ. Single-Molecule Conformational Dynamics of a Biologically Functional Hydroxocobalamin Riboswitch. J Am Chem Soc. 2014

Imlay JA. The Mismetallation of Enzymes during Oxidative Stress. The Journal of biological chemistry. 2014; 289:28121–28128. [PubMed: 25160623]

Kabsch W. XDS. Acta Cryst. 2010; D66:125–132.

Ke A, Doudna JA. Crystallization of RNA and RNA-protein complexes. Methods. 2004; 34:408–414. [PubMed: 15325657]

Keating KS, Pyle AM. RCrane: semi-automated RNA model building. Acta crystallographica Section D, Biological crystallography. 2012; 68:985–995.

Lee JW, Helmann JD. Functional specialization within the Fur family of metalloregulators. Biometals : an international journal on the role of metal ions in biology, biochemistry, and medicine. 2007; 20:485–499.

Li S, Breaker RR. Eukaryotic TPP riboswitch regulation of alternative splicing involving long-distance base pairing. Nucleic Acids Research. 2013

Ma Z, Faulkner MJ, Helmann JD. Origins of specificity and cross-talk in metal ion sensing by Bacillus subtilis Fur. Mol Microbiol. 2012; 86:1144–1155. [PubMed: 23057863]

Meyer MM, Hammond MC, Salinas Y, Roth A, Sudarsan N, Breaker RR. Challenges of ligand identification for riboswitch candidates. RNA Biology. 2011; 8:5–10. [PubMed: 21317561]

Miller, JH. Experiments in Molecular Genetics. Cold Spring Harbor, New York: Cold Spring Harbor Laborator; 1972.

Mortimer SA, Weeks KM. A fast-acting reagent for accurate analysis of RNA secondary and tertiary structure by SHAPE chemistry. J Am Chem Soc. 2007; 129:4144–4145. [PubMed: 17367143]

Nechooshtan G, Elgrably-Weiss M, Altuvia S. Changes in transcriptional pausing modify the folding dynamics of the pH-responsive RNA element. Nucleic Acids Res. 2014; 42:622–630. [PubMed: 24078087]

Nechooshtan G, Elgrably-Weiss M, Sheaffer A, Westhof E, Altuvia S. A pH-responsive riboregulator. Genes & development. 2009; 23:2650–2662. [PubMed: 19933154]

Otwinowski, Z.; Minor, W. Processing of X-ray diffraction data collected in oscillation mode. In: Carter, Charles W., Jr, editor. Methods in Enzymology. Academic Press; 1997. p. 307-326.

Pape T, Schneider TR. HKL2MAP: a graphical user interface for phasing with SHELX programs. Journal of Applied Crystallography. 2004; 37:843–844.

Peselis A, Serganov A. Themes and variations in riboswitch structure and function. Biochimica et biophysica acta. 2014; 1839:908–918. [PubMed: 24583553]

Price IR, Grigg JC, Ke A. Common themes and differences in SAM recognition among SAM riboswitches. Biochimica et biophysica acta. 2014; 1839:931–938. [PubMed: 24863160]

Quarta G, Sin K, Schlick T. Dynamic energy landscapes of riboswitches help interpret conformational rearrangements and function. PLoS Comput Biol. 2012; 8:e1002368. [PubMed: 22359488]

Que Q, Helmann JD. Manganese homeostasis in Bacillus subtilis is regulated by MntR, a bifunctional regulator related to the diphtheria toxin repressor family of proteins. Mol Microbiol. 2000; 35:1454–1468. [PubMed: 10760146]

Quisel JD, Burkholder WF, Grossman AD. In vivo effects of sporulation kinases on mutant Spo0A proteins in Bacillus subtilis. J Bacteriol. 2001; 183:6573–6578. [PubMed: 11673427]

Ren A, Rajashankar KR, Patel DJ. Fluoride ion encapsulation by Mg2+ ions and phosphates in a fluoride riboswitch. Nature. 2012; 486:85–89. [PubMed: 22678284]

Santner T, Rieder U, Kreutz C, Micura R. Pseudoknot preorganization of the preQ1 class I riboswitch. J Am Chem Soc. 2012; 134:11928–11931. [PubMed: 22775200]

Serganov A, Nudler E. A decade of riboswitches. Cell. 2013; 152:17–24. [PubMed: 23332744]

Sheldrick GM. Experimental phasing with SHELXC/D/E: combining chain tracing with density modification. Acta crystallographica Section D, Biological crystallography. 2010; 66:479–485.

Skaar EP. The battle for iron between bacterial pathogens and their vertebrate hosts. PLoS Pathog. 2010; 6:e1000949. [PubMed: 20711357]

Stahley MR, Strobel SA. Structural evidence for a two-metal-ion mechanism of group I intron splicing. Science. 2005; 309:1587–1590. [PubMed: 16141079]

Toor N, Keating KS, Taylor SD, Pyle AM. Crystal structure of a self-spliced group II intron. Science. 2008; 320:77–82. [PubMed: 18388288]

Veyrier FJBIG, Cellier MF, Taha MK. A novel metal transporter mediating manganese export (MntX) regulates the Mn to Fe intracellular ratio and Neisseria meningitidis virulence. PLoS Pathog. 2011; 7:e1002261. [PubMed: 21980287]

Waters LSS, Melissa, Storz Gisela. The Escherichia coli MntR Miniregulon Includes Genes Encoding a Small Protein and an Efflux Pump Required for Manganese Homeostasis. J Bacteriol. 2011; 193:5887–5897. [PubMed: 21908668]

Weinberg ZWJ, Bogue J, Yang J, Corbino K, Moy RH, Breaker RR. Comparative genomics reveals 104 candidate structured RNAs from bacteria, archaea, and their metagenomes. Genome Biol. 2010; 11:R31. [PubMed: 20230605]

Wilkinson KA, Merino EJ, Weeks KM. Selective 2′-hydroxyl acylation analyzed by primer extension (SHAPE): quantitative RNA structure analysis at single nucleotide resolution. Nature protocols. 2006; 1:1610–1616. [PubMed: 17406453]

Zhuang X, Kim H, Pereira MJ, Babcock HP, Walter NG, Chu S. Correlating structural dynamics and function in single ribozyme molecules. Science. 2002; 296:1473–1476. [PubMed: 12029135]

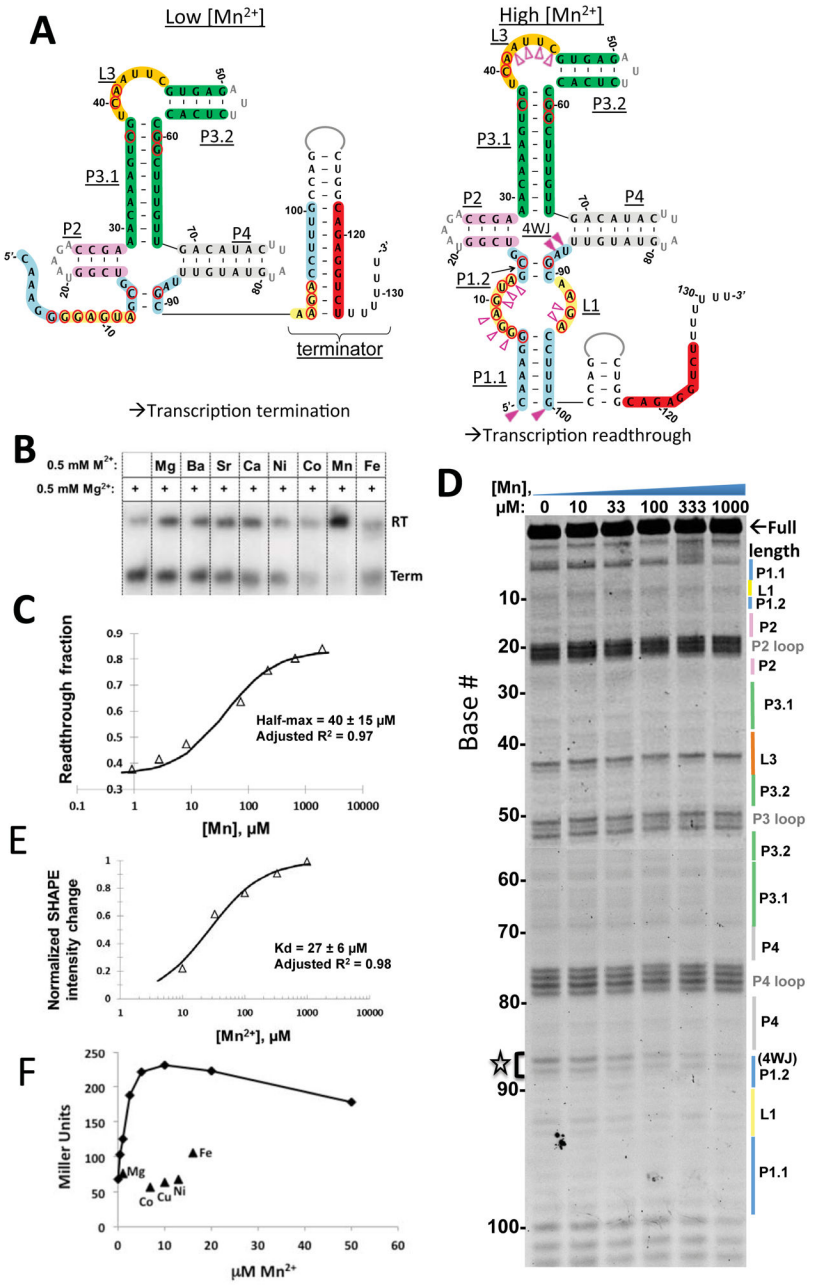

Figure 1. The *yybP-ykoY* motif is a Mn^{2+} riboswitch

A) Secondary structure of the *L. lactis yybP-ykoY* RNA showing the Mn^{2+}-dependent alternative structures. Conserved secondary structures are indicated in underlined text. Bases conserved in >94% of instances are circled in red. The 3′ halves of L1 (yellow) and P1.1 (light blue) can either form a terminator helix with complementary downstream sequence (red) or, when stabilized by Mn^{2+}, P1.1. B) IVT assay on the *L. lactis yybP-ykoY*. Products are ^{32}P labeled and separated by PAGE. Terminated (Term) products reflect terminator formation, and readthrough (RT) products result when the terminator is prevented from forming by the *yybP-ykoY* stabilization. Term and RT product sizes were confirmed on

separate gels (not shown). Mn^{2+} exhibits the largest effect. C) Transcription termination assays were performed in a range of [Mn^{2+}]. An effective k_d of 40 ± 15 μM was determined. D) SHAPE on the *L. lactis* aptamer domain under varying [Mn^{2+}]. Increased protection is observed in L1, 4WJ, and L3. E) The intensities of the SHAPE products over 87–88 were quantified and used to calculate a k_d of 27 ± 6 μM. Bases with the most drastic protections are labeled in part A with filled pink triangles; those with more subtle changes are indicated with empty triangles. F) Induction of beta-galactosidase from an *L. lactis yoaB* leader region-*lacZ* fusion in a *B. subtilis mntR* mutant strain as monitored 60 min after addition of Mn^{2+} to the indicated concentration or other metals to 400 μM.

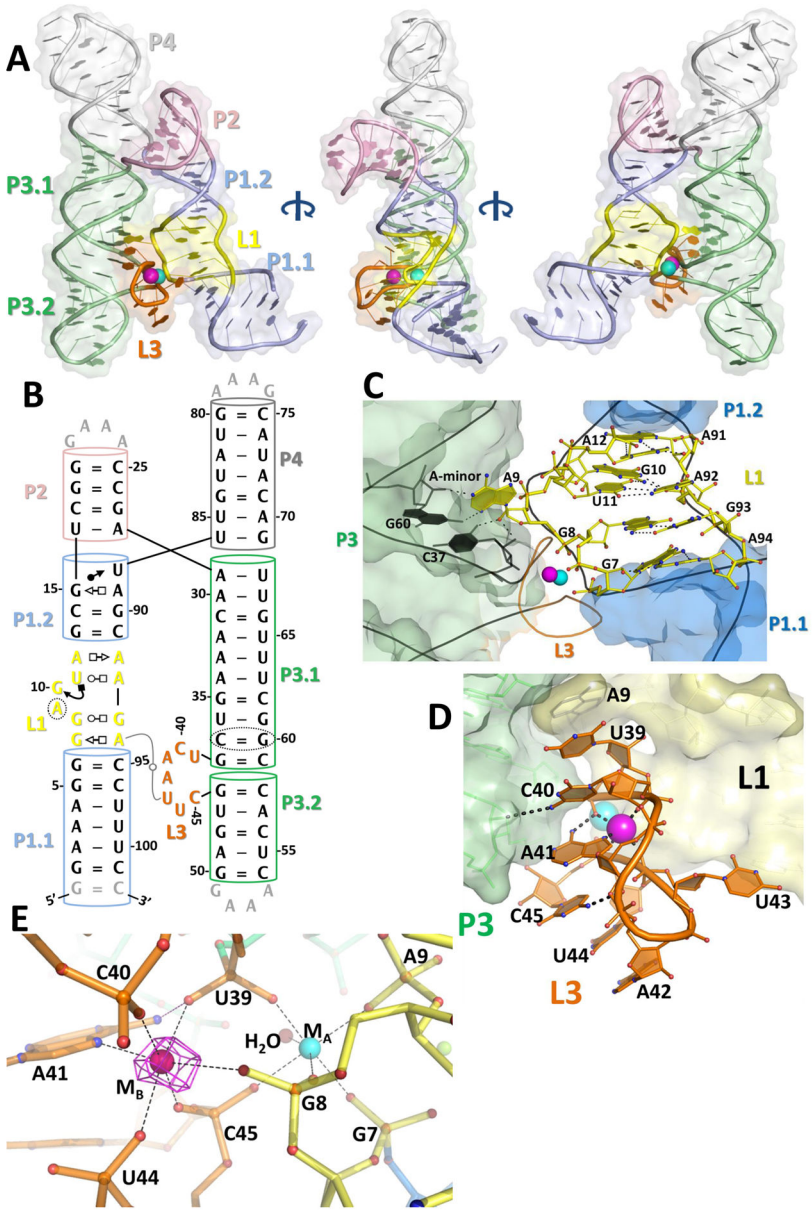

Figure 2. The crystal structure of the *L. lactis yybP-ykoY* aptamer domain bound to Mn^{2+}

A) Overall 3-D structure shows two series of coaxially-stacked helices forming an overall hairpin shape, with the highly conserved L1 (yellow) and L3 (orange) docking together and binding two metal ions (cyan and bright pink). B) Updated secondary structure reflecting the 3-D structure. Numbering is by the wild-type sequence (not crystal construct). C) The L1 region contains a series of non-Watson-Crick interactions helping to arrange the metal binding site. Notably, G7 and G8 phosphates are pointed toward the metal binding site. Additionally, A9 is flipped-out to make an A-minor interaction with C37-G60 and base stack with top of L3. D) The L3 loop contains the other half of the binding site. Extensive base stacking, and hydrogen bonds from C40 to 2′-OH of G46 and N6 of A41 to phosphoryl oxygen of U39, help arrange A41 and backbone phosphate to contact the metals. E) The

metal coordination scheme. M_A (cyan) is coordinated octahedrally by five backbone phosphates and a water. The M_B site (bright pink) contains five backbone phosphates and the N7 of A41. N6 of A41 also makes a H-bond to the phosphate of U39. The anomalous difference map collected at the Mn K-edge (magenta, contoured to 12 σ) with 100 μM Mn^{2+} confirms that M_B is Mn^{2+}-specific.

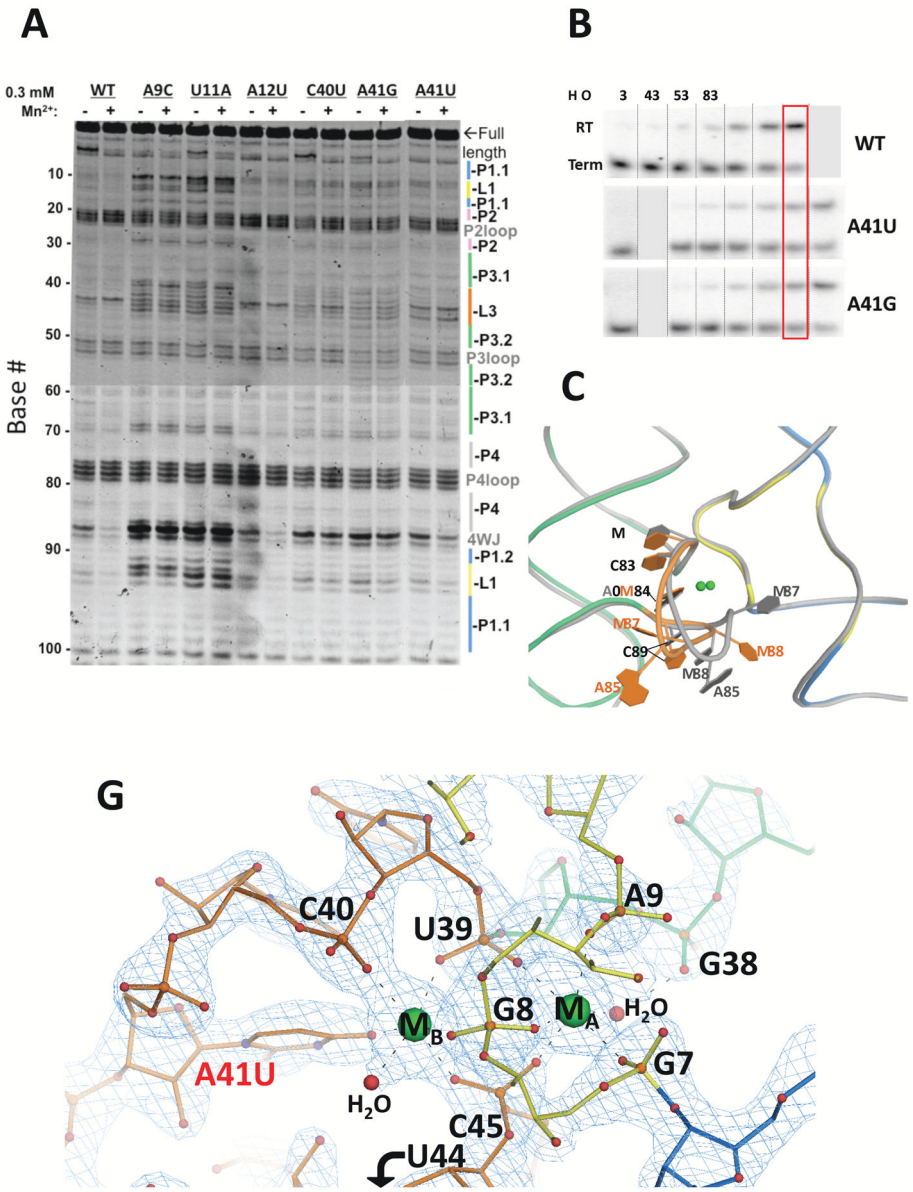

Figure 3. Mutational analysis of the *L. lactis yybP-ykoY* riboswitch

A) SHAPE with and without 0.3 mM Mn^{2+} present, on wild-type and mutant *L. lactis yybP-ykoY* aptamer domains. B) IVT assays on binding site mutants in a range of Mn^{2+} conditions. C) Overall view of the metal docking region of the A41U mutant crystal structure (colored) overlaid with the wild-type structure (gray). D) Close-up view of the A41U mutant binding site. Sr^{2+} are shown in green. The 2Fo−Fc electron density is in teal, contoured to 2.7 σ, showing a water (red) bound to M_B.

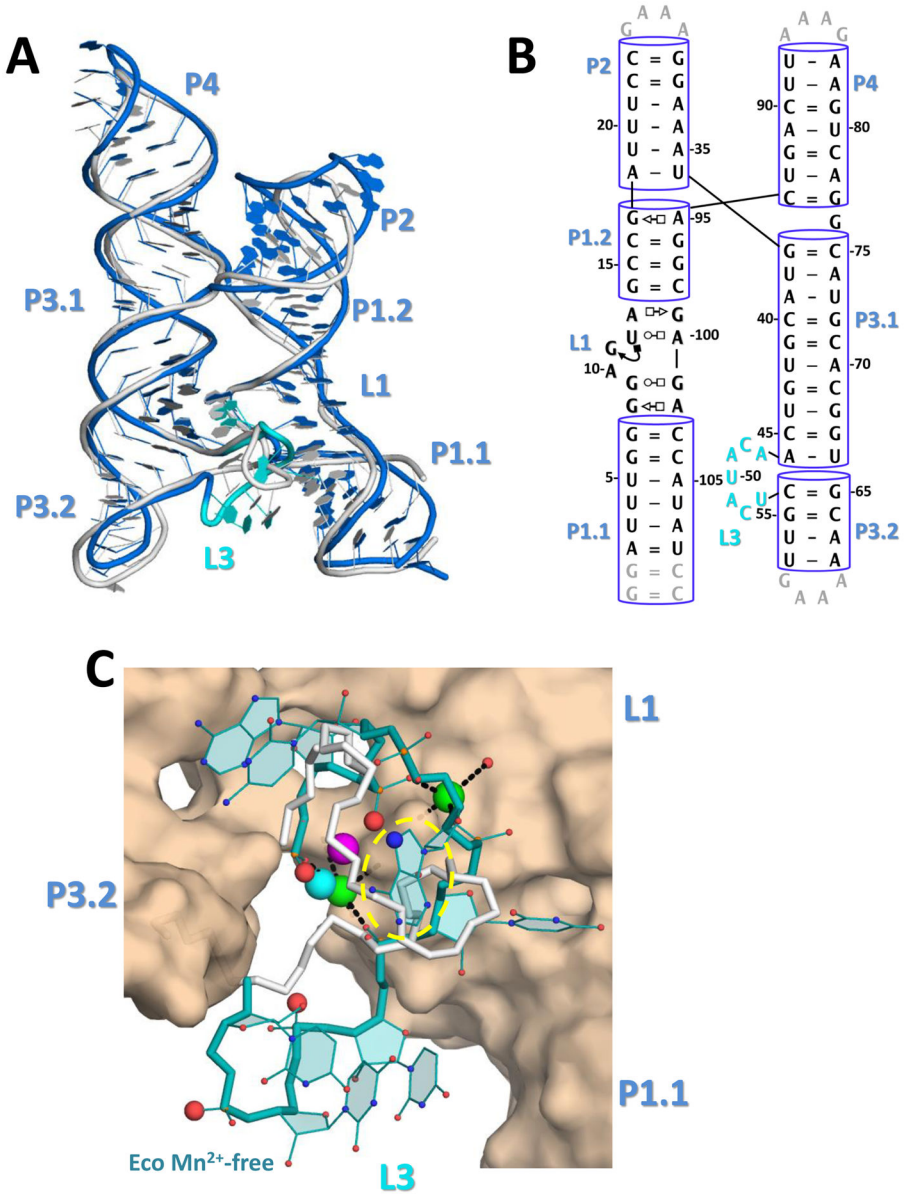

Figure 4. The Mn^{2+}-free *E. coli yybp-ykoY* aptamer crystal structure

A) Overall superposition of the *E. coli* Mn^{2+}-free molecule B (blue) and *L. lactis* Mn^{2+}-bound (gray) aptamer structures. The shifted L3 loop of the E. coli structure is in cyan. B) Secondary structure of the *E. coli* crystal structure, numbered according to wild-type sequence. C) Binding site close-up of the *E. coli* (teal) and *L. lactis* (gray) L3 loops. The *L. lactis* M_A and M_B are shown in cyan and bright pink. Two Sr^{2+} ions from the *E. coli* structure, one at M_A and one in a new site, are shown in green. The phosphoryl oxygens in the *E. coli* Mn^{2+}-free structure equivalent to those that bind M_B in the *L. lactis* Mn^{2+}-bound structure are shown as enlarged red spheres. The M_A binding site is circled in yellow.

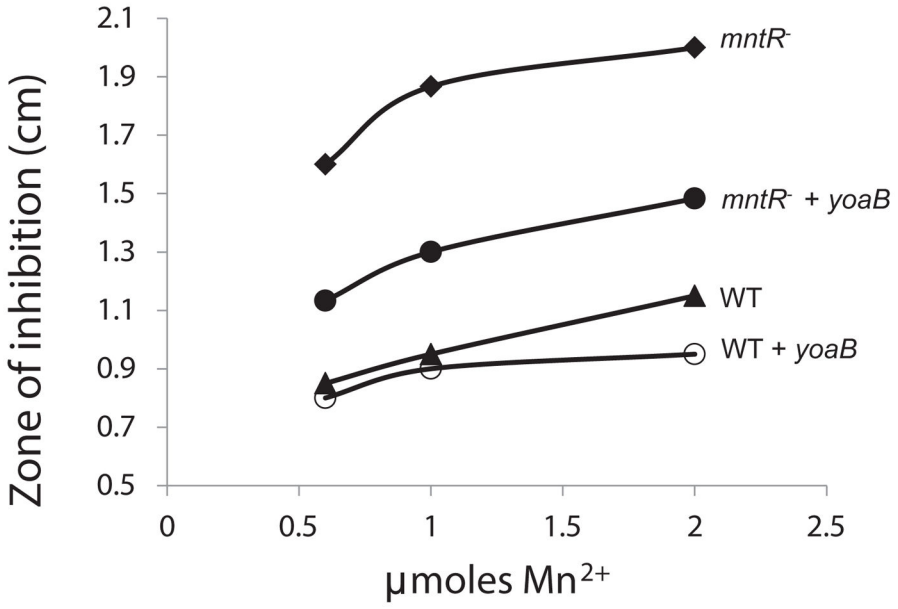

Figure 5. Rescue of Mn^{2+} sensitivity in *B. subtilis* by the *L. lactis yybP-ykoY*-associated gene *yoaB*

Sensitivity to Mn^{2+} was monitored using a disk-diffusion (zone-of-inhibition) assay. Strains were tested for the diameter of growth inhibition on LB medium amended with 1 mM IPTG (to induce YoaB expression) as elicited by exposure to 0.6, 1.0, and 2.0 µmoles of Mn^{2+} spotted on a 6 mm diameter filter paper disk. Data shown are the mean of three independent biological replicates (each tested with at least three concentrations of metals). The strains tested were wild-type (closed triangles) and the *mntR* mutant strain (diamonds), wild-type carrying *yoaB* (open circles) and the *mntR* mutant carrying *yoaB* (closed circles).

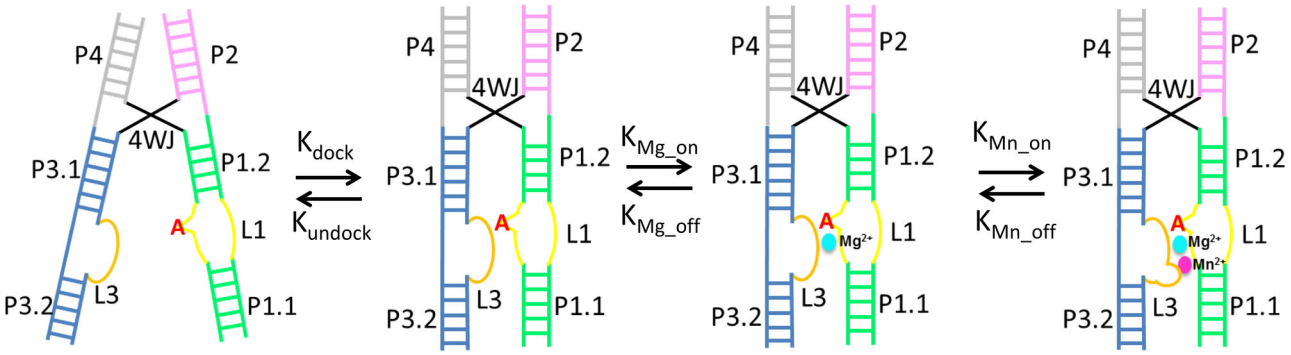

Figure 6. Hypothesized conformational switching scheme in the *yybP-ykoY* riboswitch

In the absence of Mn^{2+}, the riboswitch is in equilibrium between the undocked and docked conformation, controlled by the critical inter-helical A-minor interaction. Solution Mg^{2+} moderately stabilizes the docked conformation by mediating the L1-L3 interaction at M_A site. Mn^{2+} binding to M_B significantly stabilizes the L1-L3 interface, shifting the equilibrium toward the docked conformation.

Table 1

Crystallographic Refinement Statistics

	1 ***L. Lactis*** **IrHex**	**2** ***L. lactis***	**3** ***L. lactis*** **high [Mn^{2+}]** **(Mn edge)**	**4** ***L. lactis*** **high [Mn^{2+}]** **(below Mn edge)**	**5** ***L. lactis*** **low [Mn^{2+}]** **(Mn edge)**	**6** ***L. lactis*** **A41U** **(Sr edge)**	**7** ***E. coli*** **apo** **(Sr edge)**	**8** ***E. coli*** **apo** **(Sr inflection)**	**9** ***E. coli*** **apo** **(Sr remote)**
Data Collection									
Beamline	APS 24 ID-C	CHESS A1	APS 24 ID-C	APS 24 ID-C	**APS 24 ID-C**	**APS 24 ID-C**	APS 24 ID-C	APS 24 ID-C	**APS 24 ID-C**
Wavelength (Å)	1.1049	0.979	1.8923	1.9252	**1.892**	**0.769**	0.769	0.7692	**0.9999**
Resolution range (Å)	64.58–3.12 (3.22–3.12)	50.0 – 3.10 (3.15–3.10)	116.1–2.81 (2.91–2.81)	116.3–3.31 (3.43–3.31)	**55.9–2.85 (2.95–2.85)**	**47.4–2.24 (2.32–2.24)**	123.6–3.07 (3.24–3.07)	123.29–3.03 (3.19–3.03)	**123.6–3.0 (3.11–3.0)**
Space group	C 1 2 1	C 1 2 1	C 1 2 1	C 1 2 1	**C 1 2 1**	**P 1**	R 3 2 :H	R 3 2 :H	**R 3 2 :H**
Unit cell (a, b, c, α, β, γ)	67.0, 129.2, 114.1 90, 91.7, 90	67.3, 129.2,115.8 90, 93.1, 90	67.3, 129.2, 115.8 90, 93.1, 90	67.8, 129.7, 116.5 90, 93.5, 90	**67.3, 127.9, 115.3 90 93.37 90**	**50.4, 62.5, 70.0 116.2, 101.8, 98.8**	159.4 159.4 277.4 90 90 120	158.9, 158.9, 277.3 90 90 1 20	**159.4 159.4 277.1 90 90 120**
Total reflections	76933 (14342)	334008 (5130)	80142 (10778)	49478 (7216)	**86315 (8601)**	**102574 (10543)**	292002 (43787)	300381 (45331)	**310763 (31582)**
Unique reflections	17204 (3128)	17922 (922)	21167 (671)	14408 (1361)	**20952 (2074)**	**32334 (3300)**	25625 (3674)	26469 (3802)	**27410 (2711)**
Multiplicity	4.5 (4.6)	5.4 (5.8)	3.5 (3.5)	3.4 (2.4)	**4.1 (4.1)**	**3.2 (3.2)**	11.4 (11.9)	11.2 (11.9)	**11.3 (11.6)**
Completeness (%)	99.3 (99.2)	96.4 (98.9)	93.6 (89.1)	95.81 (91.47)	**92 (92)**	**90. (95)**	99.9 (99.9)	99.9 (99.9)	**100.0 (100.0)**
Mean I/sigma(I)	12.7 (3.2)	6.82 (1.52)	5.49 (0.90)	4.03 (0.71)	**20.5 (2.87)**	**17.6 (2.10)**	9.8 (0.9)	13.1 (1.1)	**20.2 (2.41)**
Wilson B-factor ($Å^2$)	81.60	44.48	69.00	98.80	**65.44**	**55.05**	73.19	99.56	**93.34**
R-merge	0.159 (0.649)	0.133 (0.610)	0.144 (2.35)	0.194 (1.60)	**0.136 (0.470)**	**0.053 (0.550)**	0.138 (2.992)	0.115 (2.37)	**0.116 (1.01)**
R-meas	0.181 (0.733)	0.141	0.170 (2.784)	0.231 (1.90)	**0.157 (0.539)**	**0.0647 (0.662)**	0.151 (3.27)	0.121 (2.48)	**0.122 (1.05)**
$CC_{1/2}$	0.976 (0.849)	-	0.990 (0.565)	0.988 (0.573)	**0.963 (0.945)**	**0.992 (0.722)**	0.998 (0.777)	0.968 (0.960)	**0.957 (0.943)**
Refinement									
Reflections used in refinement			21166 (669)	14406 (1364)	**20887 (2058)**	**31358 (3043)**			**27328 (2703)**
Reflections used for R-free			2074 (53)	1430 (127)	**2030 (206)**	**1741 (171)**			**1738 (172)**
R-work			0.207 (0.434)	0.223 (0.410)	**0.192 (0.393)**	**0.198 (0.336)**			**0.214 (0.324)**
R-free			0.247 (0.485)	0.256 (0.488)	**0.223 (0.428)**	**0.241 (0.417)**			**0.246 (0.376)**
Total non-hydrogen atoms			4464	4459	**4451**	**4629**			**4130**
-macromolecules			4330	4330	**4284**	**4280**			**3919**
-Ligands			59	66	**111**	**140**			**139**
RMS (bonds, Å)			0.002	0.001	**0.010**	**0.006**			**0.010**

	1 ***L. Lactis*** **IrHex**	**2** ***L. lactis***	**3** ***L. lactis*** **high [Mn^{2+}]** **(Mn edge)**	**4** ***L. lactis*** **high [Mn^{2+}]** **(below Mn edge)**	**5** ***L. lactis*** **low [Mn^{2+}]** **(Mn edge)**	**6** ***L. lactis*** **A41U** **(Sr edge)**	**7** ***E. coli*** **apo** **(Sr edge)**	**8** ***E. coli*** **apo** **(Sr inflection)**	**9** ***E. coli*** **apo** **(Sr remote)**
RMS (angles, °)			0.52	0.39	**0.46**	**1.03**			**0.73**
Clash score			2.59	3.19	**3.19**	**5.30**			**4.46**
Average B-factor ($Å^2$)			84.60	88.70	**71.46**	**57.40**			**127.26**
-macromolecules			84.30	88.40	**70.48**	**55.67**			**126.35**
-ligands			117.60	112.80	**108.89**	**95.31**			**164.86**
-solvent			78.50	80.80	**72.65**	**67.50**			**104.14**

*Where applicable, statistics for the highest-resolution shell are shown in parentheses.

*Friedel pairs were averaged when calculating reflection statistics.

*Dataset #2 was used for building an initial model, but is not shown in any figures in this study. All dataset resolutions were extended at most to shells for which CC1/2 > 0.5. Datasets used for final model refinement (bold: 5, 6, and 9) were further limited based on I/sigma(I).

*Datasets 3 and 4 were used to produce anomalous difference maps at and below the Mn edge.